Sveriges lantbruksuniversitet
Swedish University of Agricultural Sciences

Department of Soil and Environment

Size detection limits of spICP-MS for analysis of nanoparticles in environmental media

Eline Goossens

Bachelor's Thesis in Environmental Science

Examensarbeten, Institutionen för mark och miljö, SLU
2018:09

Uppsala 2018

Size detection limits of spICP-MS for analysis of nanoparticles in environmental media

Eline Goossens

Supervisor: Geert Cornelis, Department of Soil and Environment, SLU
Assistant supervisor: Jani Tuoriniemi, Department of Soil and Environment, SLU
Examiner: Dan Berggren Kleja, Department of Soil and Environment, SLU

Credits: 15 credits
Level: Basic (G2E)
Course title: Independent Project in Environmental Science – bachelor project
Course code: EX0688

Place of publication: Uppsala
Year of publication: 2018
Title of series: Examensarbeten, Institutionen för mark och miljö, SLU
Number of part of series: 2018:09
Online publication: http://stud.epsilon.slu.se

Keywords: nanoparticle, detection limit, single particle ICP-MS, environmental analysis

Sveriges lantbruksuniversitet
Swedish University of Agricultural Sciences

Faculty of Natural Resources and Agricultural Sciences
Department of Soil and Environment

Abstract

Nanoparticles (NP) are widely integrated in our everyday lives, such as consumer products, health, agriculture, food, etc. This has resulted in a growing concern for their possible harmful effect on human health and the environment and the demand for characterization. To measure the emission of NPs and exposure levels in the environment, the methods have to be able of quantifying and sizing particles of interest at parts per billion (ppb) level concentrations or lower. However, their small size and expected low concentrations against high backgrounds of naturally occurring other particles make characterization impossible with non-specific measurement techniques.

Single particle ICP-MS (spICP-MS) is a promising technique for quantification of both size and number concentration of NPs. The aim of this thesis is to evaluate the analytical capabilities of the Perkin Elmer Nexion 300 mass spectrometer for spICP-MS analysis. Gold nanoparticles were used as model NPs for all experiments and dissolved Au was added mimicking interferences or dissolved backgrounds often encountered in environmental samples. The particle size detection limit (DL) was determined and the factors determining the smallest measurable number concentration such as background count rate and particle contamination are discussed. Validation of outlier detection parameters has been done and it has been found that the more conservative n = 5 for $\mu + n*\sigma$ gives a smaller false positives count rate than the more common n = 3, while still not counting too many false negatives.

Size detection limits vary between 22 and 32 nm and concentration limits of detection (LOD) are in the range of several ng L^{-1} for smaller (40 nm) particles to ca. 40 ng L^{-1} for bigger (60 and 100 nm) particles, which is at least 10 times higher than the theoretical LOD. This made it impossible to detect particles of the size 5, 10 and 20 nm. In general, there was a lot of variation between size DLs obtained with a published equation and DLs were sometimes lower than found possible. Setting the DL to an intensity of 2 counts gave more consistent and realistic results. Adding dissolved gold (50 and 75 ppb) to artificially increase the background showed it was impossible to separate the particle events from this high background. Dwell times of 50 μs were used, but it was found that these needed to be merged to bigger dwell times to get correct results in the outlier detection algorithm. Further research to detect NPs in the presence of high dissolved backgrounds is required, as well as research for DLs and LODs of other types of nanoparticles, such as NPs with different isotopes and / or spectral interferences. Despite these shortcomings, spICP-MS has shown to be very promising for future quantification of nanoparticles in environmental media.

Keywords: Nanoparticle, detection limit, single particle ICP-MS, environmental analysis

Nederlandstalige samenvatting

Nanopartikels (NP) zijn ruim geïntegreerd in ons dagelijks leven, gaande van consument producten, gezondheid, landbouw, voedsel, etc. Dit heeft geleid tot een groeiende ongerustheid voor hun mogelijk schadelijk effect op de gezondheid en het milieu en een vraag voor karakterisatie. Om de emissie van NPs en de graad van blootstelling in het milieu te meten, moeten meetmethodes in staat zijn om de partikels van interesse te kwantificeren en hun grootte te bepalen in concentraties in een parts per billion (ppb) niveau of lager. Hun kleine grootte en verwachte lage concentraties in de aanwezigheid van hoge achtergronden van natuurlijk voorkomende, andere partikels maken karakterisatie onmogelijk met niet-specifieke meettechnieken.

Single particle ICP-MS (spICP-MS) is een veelbelovende techniek voor kwantificatie van grootte en nummer concentratie van NPs. Het doel van deze thesis is om de analytische capaciteit van de Perkin Elmer Nexion 300 massa spectrometer voor spICP-MS analyse te evalueren. Goud nanopartikels werden gebruikt voor alle experimenten als modelpartikels. De partikel grootte detectielimiet (DL) werd bepaald en factoren bepalend voor de kleinst meetbare nummer concentratie zoals achtergrond count rate en partikel contaminatie zijn besproken. De oulier detection parameters werden gevalideerd, waarbij werd gevonden dat het meer conservatieve n = 5 voor $\mu + n*\sigma$ betere resultaten oplevert dan het meer gebruikte n = 3, zonder teveel valse negatieven te tellen.

Grootte detectielimieten variëren tussen 22 en 32 nm en concentratie limieten van detectie (LOD) liggen in het bereik van enkele ng L^{-1} voor smallere (40 nm) partikels tot ca. 40 ng L^{-1} voor grotere (60 en 100 nm) partikels. Dit maakte het onmogelijk om partikels van de grootte 5, 10 en 20 nm te detecteren. In het algemeen was er veel variatie tussen grootte DLs verkregen met een gepubliceerde vergelijking en de DLs waren lager dan mogelijk. Meer realistische resultaten werden verkregen door de DL gelijk te stellen aan een partikel intensiteit van 2 counts. Het toevoegen van opgelost goud (50 en 75 ppb) om artificieel de achtergrond te verhogen toonde aan dat het onmogelijk was de partikel events van deze achtergrond te scheiden. Dwell times van 50 µs werden gebruikt, maar er werd gevonden dat deze samengevoegd moesten worden tot grotere dwell times om een correct resultaat in het outlier detection algoritme te verkrijgen. Verder onderzoek om NPs te onderscheiden in de aanwezigheid van hoge opgeloste achtergronden is vereist, net zoals onderzoek voor DLs en LODs van andere types NPs, zoals NPs met verschillende isotopen en / of spectrale interferenties. Ondanks deze tekortkomingen, is spICP-MS zeer veelbelovend voor kwantificatie van nanopartikels in het milieu.

Kernwoorden: nanopartikel, detectielimiet, single particle ICP-MS, milieu analyse

Table of contents

List of tables

List of figures

Abbreviations

(E)NP	(Engineered) Nanoparticle
(sp)ICP-MS	(Single Particle) Inductively Coupled Plasma Mass Spectrometry
AFM	Atomic Force Microscopy
AMU	Unified Atomic Mass Unit
CCT	Collision-Reaction Cell Technology
CNT	Carbon Nanotube
CPS	Counts Per Second
CVG	Chemical Vapour Generation
DC	Direct Current
DL	Detection Limit
DLS	Dynamic Light Scattering
ES-SMPS	Electrospray-Scanning Mobility Particle Size
ETV	Electrothermal Vaporization
FAST	Fast Acquisition Speed Technique
FCS	Fluorescence Correlation Spectroscopy
FlFFF	Flow Field Flow Fractionation
ITE	Ion Transmission Efficiency
LOD	Limit Of Detection
NTA	Nanoparticle Tracking Analysis
PMF	Probability Mass Function
PPB	Parts Per Billion
PSD	Particle Size Distribution
RF	Radio Frequency
sdFFF-DLS	Sedimentation FFF hyphenated with DLS
SF	Sector Field
TEM	Transmission Electron Microscopy
TOF	Time of Flight

WWTP	Wastewater Treatment Plant

1 Introduction

Nanoparticles (NPs) are currently everywhere in our everyday lives, from silver NPs in fabrics to limit bacterial growth to silicate NPs in food packaging to slow down the process of spoiling or drying out (Boysen and Boysen, 2018). The number of applications in consumer products are steadily increasing. Due to their large surface area to volume ratio NPs have increased intermolecular and surface forces compared to the corresponding bulk material. This increases their solubility and reactivity and therefore also possibly their toxicity. The electronic structure also differs from that in the bulk material because the number of interacting atomic orbitals in a small particle is not close to infinite. This has a profound consequence on *e.g.* the optical properties with the absorbance and fluorescence frequencies increasing when the band gap becomes wider with decreasing particle size. Small particles can be taken up by cells via endocytosis and diffuse through biological membranes while they stay dispersed longer and are therefore more mobile in the environment. Because the behaviour in environmental compartments is molecule-like, NPs should be subject to the same safety regulations and risk assessment procedures as are molecular and ionic substances (Wiesner et al., 2006, Westerhoff and Nowack, 2012, Hassellöv et al., 2008).

Consequently, questions have been raised about their safety in consumer products. The potential risks on human health and the environment are still poorly understood (Nel et al., 2012, Handy et al., 2008). In particular, the toxicity as a function of concentration on both humans and organisms upon prolonged exposure needs more investigation.

The EU-definition of nanomaterials is as follows: (EuropeanCommission, 2017)

> Nanomaterials are a natural, incidental or manufactured material containing particles, in an unbound state or as an aggregate or as an agglomerate and where, for 50% or more of the particles in the number size distribution, one or more external dimensions is in the size range 1 nm - 100 nm.
> In specific cases and where warranted by concerns for the environment, health, safety or competitiveness the number size distribution threshold of 50% may be replaced by a threshold between 1 and 50%.

Correct implementation of this definition requires techniques that can quantify particles in the 1 – 100 nm range by determining number-based size distributions. Quantification of the NP size is needed because NPs behave different than their dissolved state and different than the bulk material. Due to the low concentrations of NPs in the environment (in the range of 10^{-13} to 10^{-8} g L^{-1}) in complex matrices and the low toxic effect levels found for some NPs, this method needs to be both sensitive and selective. Sensitivity is needed because small differences in NP size and number concentration can lead to big differences in toxicity, while the selectivity is needed to adequately distinguish the NPs present, as each NP has a different toxicity level. On top of this, the technique needs to be fast enough for routine applications. Out of all analytical techniques that currently exist, spICP-MS is the only one that ticks all the boxes.

spICP-MS essentially using the ICP-MS instrument as an element specific single particle counter quantifying the ion bursts coming from individual particles ionised in the plasma. Relevant NPs often consist of trace elements (*e.g.* Ag, CeO_2, WC, $Cr(OH)_3$) that can be detected at number concentrations as low as 10 – 100 particles mL^{-1} in the presence of orders of magnitude higher concentrations of natural background particles, mostly consisting of silicate materials, biological debris and iron oxides (Bustos and Winchester, 2016, Gallego-Urrea et al., 2010).

Single particle ICP-MS was first described in a series of papers by Degueldre *et al.* published between 2003 and 2006 (Degueldre and Favarger, 2003, Degueldre and Favarger, 2004, Degueldre et al., 2004, Degueldre et al., 2006a, Degueldre et al., 2006b). Since this initial suite of papers demonstrating the proof of principles of the technique, researchers have developed methods for absolute measurement of number concentrations and particle sizing based on calibration with dissolved standards.

1.1 Inductively Coupled Plasma Mass Spectrometry (ICP-MS)

Inductively coupled plasma mass spectrometry (ICP-MS) is a powerful technique for the detection of trace and ultra-trace elements. It is based on the general principle that an analyte sent through a plasma where temperatures can reach 6000 K will be atomised and partly ionised. The singly charged positive ions are separated based on their mass by a mass spectrometer and are in general detected by an electron multiplier detector.
ICP-MS has low limits of detection for concentration (LOD), ranging from μg/L to ng/L. Heavier elements have in general lower LODs. For example, Au has a reported limit of detection (LOD) of 0.9 ng/L and Ag 2.0 ng/L on a quadrupole mass spectrometer. ICP-MSs are equipped with electron multiplier tube detectors capable of both pulse counting and analogue detection, which gives them a wide dynamic range spanning over 6 orders of magnitude. It is possible to measure almost every isotope. Sector field (SF) instruments have the best resolution for this, while the more common quadrupole spectrometers are prone to isobaric interferences. Multicollector or time of flight (TOF) ICP-MS are also capable of measuring several elements simultaneously, meaning they only need a couple of ns to measure more elements instead of quadrupoles and SFs that require several ms.

An ICP-MS system consists of the following parts, that will be discussed in more detail: the sample-introduction system, the plasma source, the interface region and ion focusing system, the mass spectrometer and the detector (Thomas, 2001c).

1.1.1 The sample-introduction system

The samples analysed are usually liquids. Liquid samples must be introduced to the plasma as fine aerosols to facilitate ionization without extinguishing the plasma. The sample introduction system therefore consists of a nebulizer, and a spray chamber for removing large droplets that could destabilize the plasma, and dampening fluctuations in the sample flow, which would otherwise lead to drift and fluctuations in the signal intensities.

The sample is pumped by a peristaltic pump into the nebulizer that generates the aerosol. The most commonly used type of nebulizers is pneumatic, where the aerosol is created by an Ar gas stream.

The two basic types of pneumatic nebulizers are the concentric, where the liquid sample jet is surrounded by a parallel concentric gas stream and breaks into droplets as it expands into the low-pressure environment generated by the Bernoulli effect of the rapidly moving gas, and crossflow, where the sample is directed to an orthogonal gas stream and becomes nebulized as they are mixed inside a capillary.
The benefit of crossflow compared to concentric is that the liquid capillary has a larger inner diameter, allowing larger particles at higher concentrations to pass through. However, the produced droplets are larger and more polydisperse than those from a concentric nebulizer, which decreases precision and increases interferences (Montaser, 1998).

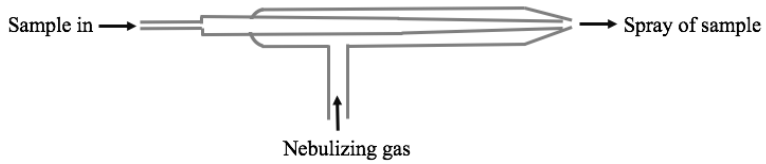

Figure 1. Schematic representation of the concentric nebulizer

The produced aerosol then passes through the spray chamber. It only allows the fraction of the droplets that is smaller than a few microns to proceed to the plasma, while the rest of the polydispersive aerosol is being discarded as waste. It also smooths out the periodic pulses in sample flow that are often caused by the peristaltic pump. The double-pass spray chamber mostly uses the Scott design. In this design, the aerosol must pass two baffles between which the larger droplets fall out by gravity while travelling the length of the spray chamber. Another type is the cyclonic spray chamber, which is a cylinder where the aerosol is blown in from the nebulizer in such a way that it creates a vortex that casts the larger droplets on the walls by centrifugal force. The waste is pumped out from the bottom of the cylinder while the finest fraction of the aerosol proceeds to the plasma through a tube at the top of the spray chamber (Thomas, 2001d).

While it is not of importance for conventional ICP-MS, the nebulization efficiency (also known as transport efficiency) is an important parameter in spICP-MS calculations. This is the fraction of sample entering the nebulizer that eventually passes the spray chamber into the plasma. Reported nebulization values vary between 1 – 10%, but high-efficiency nebulizers can get much higher values. They depend on the nebulizer and spray chamber, but also on parameters such as gas flow rate, viscosity and uptake rates (Pace et al., 2011). A higher nebulization efficiency leads to more particles entering per dwell time and can consequently lead to lower LODs. Methods of calculating the nebulization efficiency are explained in section 1.2.5.

Sample introduction systems are constantly plagued by memory effects. A certain level of analyte signal remains after the rinsing following analysis, and only slowly decreases when pumping clean solutions into the mass spectrometer. Some analytes such as Au, Ag, Hg, B, Zn etc. are notoriously 'sticky' because they adhere to the walls of the spray chamber and transfer tubing. Washout times for these elements can however be reduced by adding sulphur containing complexing agents such as cysteine or thiourea. These are soft Lewis bases, which are preferred ligands for coordination with soft Lewis acids such as Au, Ag Hg etc. The coordinated species are then less vulnerable to decomposition in the acid solutions and prevent interaction between the analyte and the surface of the sample-introduction system (Chen et al., 2000). Adding these complexing agents reduces the dissolved background caused by memory effects and can lead to lower DLs.

1.1.2 The plasma source

The plasma is operated at approximately 6000 K, so when the injected sample reaches the plasma, it is dried, vaporized, atomized and partly ionized. The plasma source comprises the ICP torch, the RF (radio frequency) coil and a RF power supply. The power supply occurs by power oscillators (also known as free-running oscillators) or power amplifier/oscillator combinations (also known as crystal-controlled generators).

The ICP torch consists of three concentric tubes usually made of quartz: the outer tube, the middle tube and the sample injector, as can be seen in figure 1. They are wrapped at one end by a RF coil. Argon is generally used for generating the plasma, since it is abundant (thus cheaper than the other noble gases) and has a higher first ionization potential than every other element (with the exception of He, Ne and F). This means recombination of an electron with the argon ion is more energetically favourable than with the analyte ion (Lias and Liebman, 2018). In other words, the analytes will be ionised more than the make-up Argon gas. Argon gas is also used for generating the plasma flows between the outer and middle tubes. Between the middle tube and the sample injector flows an auxiliary gas that can be used

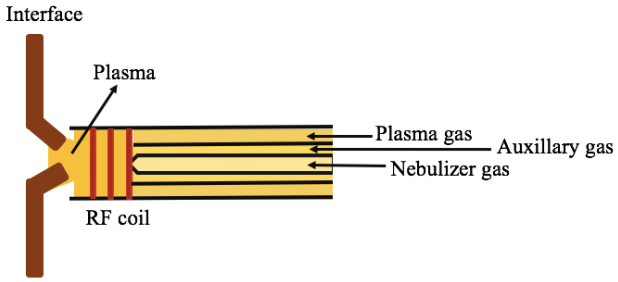

Figure 2. Schematic representation of the plasma source

for controlling the position of the base of the plasma. The nebulizer gas, carrying the sample aerosol, flows faster than the plasma gas and pierces a channel through the auxiliary plasma.
A high-voltage spark through the gas initiates the plasma by ejecting some electrons and giving them enough energy to undergo inelastic collisions with the argon atoms. The plasma is sustained by applying a RF power (usually 750 - 1500 W) to the RF induction coil, creating a high-frequency oscillating electromagnetic field that accelerates the free electrons. They collide with additional argon atoms, creating an avalanche effect where even more electrons are released and a plasma discharge is formed. Both the positively charged argon ions and the electrons are accelerated, but the smaller electrons reach much higher velocities and are dominating the energy transfer processes in the plasma. A steady-state plasma is obtained when the rate of which electrons are removed from argon atoms by collision is equal to the rate at which these electrons are lost by recombination. This entire chain-reaction takes place in only a couple of milliseconds (Montaser, 1998).

The gas beam first maintains charge neutrality, until the more mobile electrons tend to leave the beam due to charge diffusion and electrostatic repulsion. As the beam becomes positively charged, it expands due to electrostatic repulsion. Because of this space charge effect lighter elements are more prone to be ejected to trajectories off axis from the skimmer cone, and a bias towards heavier elements is introduced into the mass spectrum, because heavier elements are rejected less (Montaser, 1998).

1.1.3 The interface region and ion focussing system

The mass spectrometer works under vacuum, but the plasma operates under atmospheric pressure. Hence, an interface is needed where the ions are transported with minimal losses and with electrical integrity to the lower-pressure zone.
The interface region consists of the coaxial and water-cooled sampler and skimmer cones, through which the plasma gas flows to zones with sequentially decreasing pressure, and the ion optics located behind the skimmer cone for extracting and forming a beam of the positive ions and sending them to the mass analyser. The jet of plasma gas exiting through the sampler cone expands cylindrically at a supersonic speed due to the sharp fall in pressure. The expansion continues until collisions with the residual gas slows down further expansion and spatially confines the gas beam (Vanhaecke, 2017). The ion focusing system is located behind the skimmer cone and consists of a series of metallic plates, barrels or cylinders under voltages. Their role is to guide the maximum number of analyte ions into the quadrupole, while

making sure that neutral species and photons are rejected from the ion beam (Thomas, 2001a). The more ions will enter the quadrupole, the higher the size DL.

1.1.4 The mass spectrometer

The mass spectrometer separates ions according to their mass-to-charge ratio (m/z). The most commonly used mass analyzer, that is also installed on the mass spectrometer used in this thesis, is the quadrupole mass filter. It can work at relatively high pressures and has a good tolerance to the energy spread of ions entering. However, it has lower mass resolution compared with for instance the more expensive sector field design.

A quadrupole consists of four parallel cylindrical or (more ideally) hyperbolic metallic rods of the same length and diameter. Opposing rods are connected together to form electrode pairs, one under a direct current (DC), and the second under a radio frequency (RF) voltage applied (figure 3). Only the ions with a certain m/z ratio will follow a path through the quadrupole reaching the detector, the others will follow an unstable trajectory and are ejected. The m/z ratio capable of passing the quadrupole is determined by the ration between the applied DC and RF voltages (Thomas, 2001b).

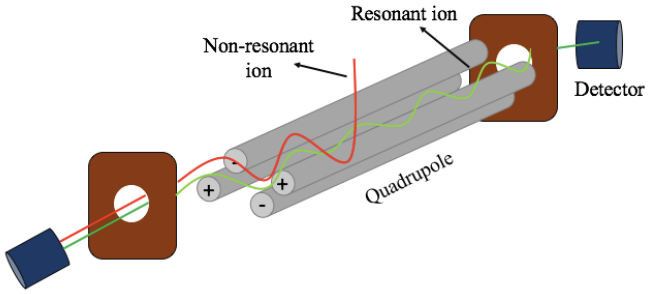

Figure 3. Schematic representation of the quadrupole mass analyzer

The measures of quadrupole performance are the resolution and the abundance sensitivity.
The resolution (also called resolving power) is the ability of the mass analyzer to separate two adjacent peaks. The resolution R is defined as:

$$R = \frac{m}{\Delta m}$$

with Δm = the width of the peak at mass m on 5% of its maximum height. Typical quadrupole resolutions vary between 0.7 and 1.0 amu (unified atomic mass unit) (Thomas, 2001b).

The abundance sensitivity is usually defined as the ratio of intensity in counts per second (cps) of the peak tail measured at mass *m - 1* or *m + 1* to intensity in cps of the peak measured at mass *m* (Boulyga and Becker, 2002). The value is dependent on the resolution: generally, the higher the resolution, the lower the sensitivity.
Sensitivity is usually of less importance for spICP-MS, since the peaks are sufficiently separated from each other due to low concentrations.
However, better resolution does improve the DL in spICP-MS. Because of the low mass resolution, a quadrupole can only completely resolve ions with a mass difference of at least 0.5 amu. Otherwise, both ions will simultaneously contribute to the signal. This is called isobaric, or spectral interference. It can occur between any combination of atomic, molecular or doubly charged ions that have nearly equal mass to charge ratio. While there are ways to minimize the occurrence of spectral interferences, they are never 100% avoided. This is less of a problem for ^{197}Au, which only interference is $^{181}Ta^{16}O^{+}$ (May and Wiedmeyer, 1998), but it increases the size DL for other, more interfered NPs. In this thesis, dissolved gold is added to NPs to mimic the occurrence of spectral interferences.

One option to improve the size DL in spICP-MS is to increase the ion transmission efficiency (ITE), which is the fraction of particles entering the plasma that are detected by the mass spectrometer. ITE values are usually < 0.1%, but it is believed that with an ITE of ca. 10%, Ag NPs of only 1 nm could be detected with a sector-field ICP-MS (Tuoriniemi et al., 2015). The ITE is instrument-specific and depends on the interface region and the mass spectrometer.

The quadrupole is a mass filter that only allows ions with a m/z that lies in a narrow 'window' of less than 1 amu to pass. By continuously adjusting the applied current, this window can scan over a complete mass reach, giving a mass spectrum as a result. This is called scanning. Another method is called peak hopping or peak jumping, where the voltages are changed abruptly to jump between selected isotopes.
Other mass analyzers include the double focusing magnetic sector, time-of-flight (TOF) and collision-reaction cell technology (CCT).

1.1.5 The detector

The electron multiplier detector records either current pulses coming from individual ions hitting the detector, or at higher count rates, a current that is proportional to the flux of ions which is then usually recalculated to count rate expressed in counts per second (cps). This way, it counts all the individual ions exiting the quadrupole, providing a result in counts per second (cps). The ions striking the detector are converted to current pulses by a series of dynodes with a negative potential at the front and the back side kept at ground for the detection of positive ions. The dynodes are coated with a semiconductor that emits one to three electrons when an ion strikes the surface. These so-called secondary electrons are accelerated from dynode to dynode each time emitting more electrons creating an avalanche effect. The electrons are absorbed by a metal anode at the end. The result is a discrete pulse of millions of electrons generated by one ion hitting the detector.

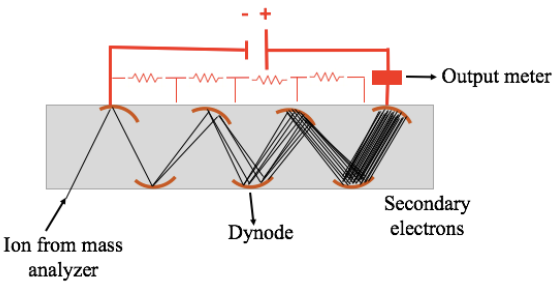

Figure 4. Schematic representation of the discrete dynode detector

The detector can operate in pulse counting mode, which counts the separate pulses, or at high count rates in analogue mode, measuring the current flowing through the detector (Thomas, 2002, Vanhaecke, 2017). spICP-MS detectors only operate in pulse counting mode.

1.2 Single particle ICP-MS (spICP-MS)

1.2.1 Data acquisition and dwell time

The main difference between operating an ICP-MS instrument in conventional and in spICP-MS mode is that in the latter considerably shorter dwell times are used. A typical particle event can be described as a roughly Gaussian shaped burst of ions with a standard deviation of 100 - 200 µs. If one uses dwell times of > 100 ms that are typical for conventional data acquisition, the number of background counts from dissolved analyte and dark current is likely to overwhelm the ion bursts from the particle and there is a high risk of coincidence.

As the dwell time is shortened, the background signal decreases while the particle signal remains the same. The smallest particle size that can produce a detectable pulse in signal thus decreases in intensity with shortening dwell time until 100 - 200 µs, from where usually no further improvement in size DL is obtained by shortening the dwell time. The dwell times used for spICP-MS are almost invariantly < 20 ms.

Another requirement of spICP-MS is that only one particle at a time enters the plasma during a dwell, since otherwise multiple particles would be counted as one, and the calculated particle sizes would be overestimated while the number concentration is underestimated. The risk of coincidence decreases with shortening dwell time and decreasing concentration.
The longer the dilution, the longer the analysis time required for acquiring a statistically significant number of particle events, and shorter dwell times entail larger datasets to be processed. In addition, in many instruments the data acquisition is discontinuous, meaning there is a gap between the dwells. In such case particle events might become incompletely measured if the ion burst does not fully coincide with the dwell, the risk therefore increasing with shortening dwell time. The fraction of multiple particle events in a measurement can be predicted and corrected for using Poisson statistics (Tuoriniemi et al., 2018). Models for accounting for the occurrence of incomplete particle events have also been devised in literature (Tuoriniemi et al., 2014).

Shortening the dwell time increases the number of data points that needs to be processed. The choice of dwell time and dilution of the sample to a concentration suitable for measurement are therefore critical aspects of the method.
When dwell times are longer than the duration of a NP event the main problem is particle coincidence, that is two or more particles arriving during the same dwell (figure 3) (Tuoriniemi et al., 2018, Kutscher et al., 2018). This artefact can become severe when particle number concentration is high.

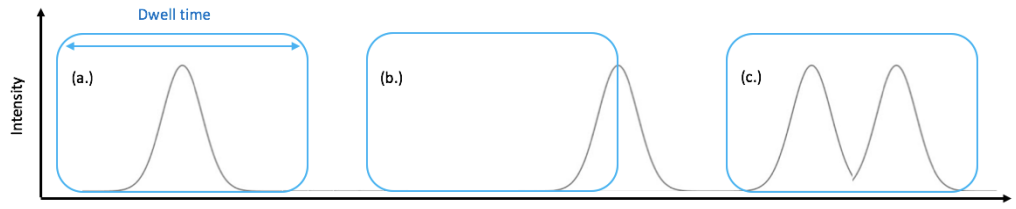

Figure 5. Illustration of data acquisition. (a.) One particle event detected during the dwell. (b.) Split event: particle event is only partially detected in the dwell. (c.) Coincidence: two particle events detected in a single dwell.

The analysis is affected by the noise levels in the background signal. Background fluctuations could be confused with particle events of comparable magnitude. Therefore, algorithms that could either be based on outlier detection or deconvolution of the dissolved and particulate signals from each other are needed for detecting and quantifying the particles. Reducing the dwell time to durations comparable to that of the particle events improves size detection limits as the background signal and its noise becomes lower. As mentioned, further shortening from ~200 µs also reduces the particle signal in each dwell and therefore does in most cases not produce any gain. Because the risk of overlap between particle events is reduced, this FAST (Fast Acquisition Speed Technique) discussed by Tuoriniemi *et al.* (2015) and Montano *et al.* (2014) can also characterize more concentrated dispersions.

1.2.2 Size DL in spICP-MS

In 2014 Lee *et al.* (2014) published an equation for predicting the DL for spICP-MS for each element based on the sensitivities and noise levels in blank signals. It is practical because, knowing the mass spectrometer sensitivity, it can be predicted whether spICP-MS analysis of a given sample is feasible without carrying it out. Furthermore, they demonstrated that the use of collision cell technology (CCT) decreases the DL for Fe NPs by supressing the isobaric interferences that reduce Fe sensitivity.
The reported equation for calculating the size DL is:

$$DL = \sqrt[3]{\frac{6 \times 3\sigma_{DI}}{R \times f_a \times \rho \times \pi}} \qquad (1.)$$

where 3σ = the magnitude of the background noise (counts), R = the sensitivity of the detector for the elements in the analyte (counts g^{-1}), which is the slope of the calibration curve that plots the mass entering per dwell (g) in function of the intensity (counts), f_a = the mass fraction of the analysed element in the NP and ρ = the density of the NP (19.30 g cm^{-3} for Au).

The dissolved background in the sample needs to be separated from the particle signal, which is often based on a $\mu + n\sigma$ threshold, where σ is the standard deviation of the whole dataset. Since the dissolved signal can only approximately be described by any probability function, a multiple of the standard deviation will never exactly correspond to a given probability for falsely identifying a particle event. A NP intensity with a 3σ threshold has been adopted in many articles (Mitrano et al., 2012), since in a Gauss curve 99.7% of the values lie within $\mu \pm 3\sigma$. Equation (1.) is based

on this 3σ threshold, by calculating it repeatedly until no extra particle signals are set apart. It has been calculated that 0.13% of a Gaussian distributed dissolved signal is falsely counted as particles within this threshold. However, a Poisson distribution is deemed to be more appropriate for describing background signals, in which case ~ 0.5% of data points are falsely counted (Laborda et al., 2013, Tuoriniemi et al., 2015). For this reason, a 5σ threshold is sometimes regarded as more appropriate.

Tuoriniemi *et al.* (2012) investigated the detection limits (DL) of spICP-MS for size and number concentrations with Ag NPs (ca. 20 - 80 nm). An iterative algorithm was presented for distinguishing the particles as outliers against a continuous dissolved analyte background. A particle event is detected as an outlier if its intensity exceeds the average signal by more than 5 times its standard deviation. The particle events detected this way are removed from the signal, and the algorithm is repeated until no new particle events are found. The dwell time was optimised to 5 ms at which the smallest detectable particle size was ~20 nm for Ag. This DL is mainly limited by the overlap of particle events and dissolved signal that increases with the background signal noise.

Using dwell times shorter (~ <500 µs) than the particle event duration has the advantage of that the size DL improves because the background signal and its noise decreases. Higher number concentrations can be characterized because of the lower risk of overlap between the ion bursts. The accuracy of detector dead time error correction improves, because the count rate due to particle signal fluctuates less during each dwell. This fast acquisition speed technique (FAST) and an adaption of the iterative outlier detection algorithm for such datasets was discussed in a recent article by Tuoriniemi *et al.* (2015). A standard deviation of 5 was again regarded as a compromise between low frequency of false positives (contribution of false positives is < 0.1% of actual particle events) without eliminating too many actual particle counts. At close to optimal dwell times (100-200 µs) the Au and Ag detection limits were limited by the ion transmission efficiency (ITE) of the instrument.

Another method for distinguishing the NP signals from the background is the deconvolution method by Cornelis and Hassellöv (2014). This method fits Polyagaussian probability mass functions (PMF) to signal distributions of blanks and dissolved standards with known concentrations. Thus, the PMF of the dissolved signal is known, and can therefore be deconvoluted from that of the combined signal. The possibility to quantify particle signals overlapping with the background can substantially reduce the size detection limit.

1.2.3 Calibration methods

The simplest way of calibrating the spike intensities for particle size would be a plot of the signal intensity against the diameter of particle size standards. This would, however, require that a set of size standard NPs is available for all chemical compositions of interest. Furthermore, calibrating the particle frequency for number concentration would require reliable standards for this measurement, which are not yet available for any material (Montano et al., 2016).
A more feasible approach that is used almost invariantly to determine the nebulization efficiency, and then determine the sensitivity in terms of counts per mass of element entering the plasma from a calibration curve of dissolved standards. The equation that is used for relating the dissolved concentration to the total analyte mass entering the plasma was given by Pace *et al.* (2011):

$$I = S \times C_{STD} \times f_{neb} \times Q_{sample} \times t_{dwell} \quad (2.)$$

with I = intensity (counts) in a dwell, S = sensitivity in counts per mass entering the plasma (g^{-1}), C_{STD} = concentration (g mL^{-1}), f_{neb} = nebulization efficiency, Q_{sample} = flow rate (mL s^{-1}) and t_{dwell} is the dwell time (s). The measured intensity is related to the mass delivered by the dissolved standards in each dwell, so the mass of the analyte in the NP can be calculated by $I_{nanoparticle}/S$.
These calibration curves with dissolved standard can be used to determine particle size distributions (PSD), which plot the frequency (particles nm^{-1}) vs the diameter of the particle (nm). There is a risk that the f_{neb} for the solvent, dissolved analyte and NPs differ, although this matter remains poorly investigated.

1.2.4 Particle size distribution

There are some steps that need to be taken to obtain the PSD from the raw data. The procedure is outlined in figure 4. As mentioned before, the raw data consists of a sum of the signals from the particles and a continuous background due to dissolved analyte. The particle events can be distinguished by applying a detection threshold, so only intensities surpassing this threshold are considered as particle events. The average background intensity of the dwells not containing particles is subtracted from the combined signal in particle containing dwells to remove any contribution from dissolved species from the PSD.

There are two procedures to set this threshold. The first is the iterative algorithm that distinguishes outliers from the dissolved background when they exceed I_{mean} + $n*\sigma_{signal}$ (Tuoriniemi et al., 2012), as described in section 1.2.2.
The second outlier detection algorithm is the *k*-means clustering algorithm, which divides the data into k groups. Each data point is assigned to a group in a way that the sum of the distances of all data points to each peer in their respective group is minimized. The value for *k* is again chosen manually. This method has, however, only been discussed in a single paper and its capabilities have not yet been sufficiently assessed for it to be applied on analytical tasks (Bi et al., 2014).
Another way of distinguishing the particle events is the method of deconvoluting the dissolved and particulate signals using the method by Cornelis and Hassellöv (2014).

To get to the PSD, the corresponding diameter for every intensity in the frequency-intensity diagram needs to be calculated. First, the following equation is used to calculate the mass of the particle:

$$M_P = \frac{1}{f_a} \frac{I_{NP} - I_{BKGD}}{s} \tag{3.}$$

with M_P = mass of particle (g), f_a = mass fraction of analyte in particle and s = sensitivity (counts g^{-1}). The sensitivity is determined from the calibration plot of intensity vs. amount of dissolved analyte that enters the plasma during each dwell that is constructed based on equation (2).
With this result, and relying on the assumptions that the particle density is constant and equal to the bulk density and the shape is spherical, the diameter of the NP can be calculated from:

$$D_P = \sqrt[3]{\frac{M_P \times 6}{\rho \times \pi}} \tag{4.}$$

with D_P = diameter of particle and ρ = density.

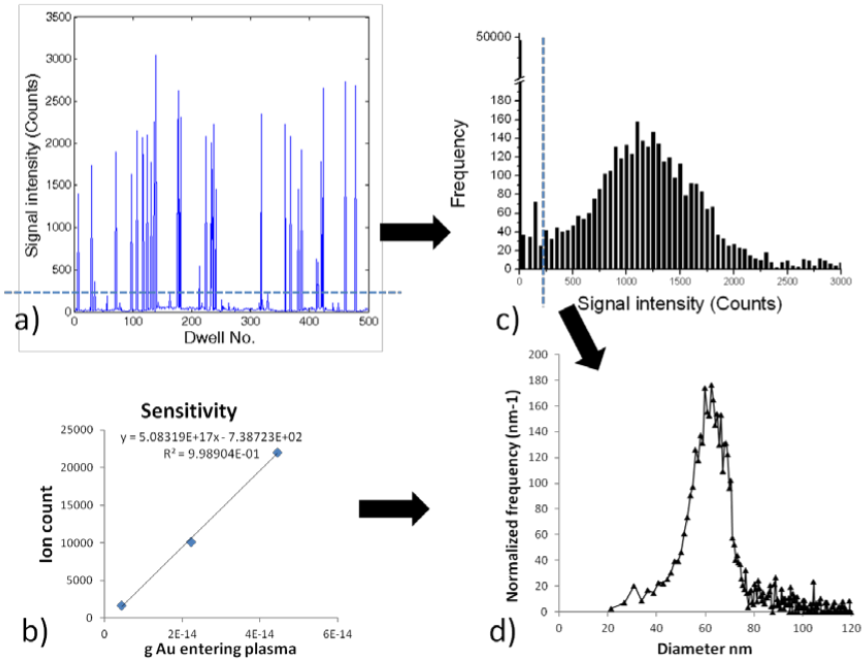

Figure 6. Process of calculating the PSD from the raw data. ***a)*** *Raw data: signal intensity (counts) of a series of dwells. The dotted horizontal line is the detection threshold.* ***b)*** *Calibration curve of signal intensity (counts) against mass of analyte entering the plasma per dwell.* ***c)*** *Data from a) is replotted in to a frequency intensity diagram.* ***d)*** *Data from c) is replotted into a particle size distribution. Figure reproduced with permission from the author from ref. (Tuoriniemi et al., 2018)*

There is a linear relationship between the frequency of NP events and the number of NPs per volume unit in the sample, which can be used for calculating the number concentration c_p (equation 5), provided the nebulization efficiency is known (Tuoriniemi et al., 2018).

$$C_P = \frac{f(I_P)}{f_{neb} \times q_{neb}} \quad (5.)$$

with $f(I_p)$ = frequency of NP events and q_{neb} = sample uptake rate (mL s^{-1}). The arrival of particles into the plasma has shown to be random (Tuoriniemi et al., 2014).

1.2.5 Nebulization efficiency

As earlier mentioned, a parameter called the nebulization efficiency needs to be determined for calculations. A particle remains intact until it enters the plasma and the mass of this particle, that is eventually related to its size, is therefore independent of the volume that travels with it. However, the total mass of the dissolved standards is depended on the concentration and thus the volume that travels to the plasma during each dwell. Since dissolved standards are used to relate intensity to particle

mass, the nebulization efficiency is used to convert concentration to particle mass entering per dwell, because it accounts for the volume loss during transport through the spray chamber.
There are three methods described for determining this parameter, as described by Pace *et al.* (2011) and Montano *et al.* (2016):

1. The waste collection method:
For this method, the spray chamber waste that does not go into the plasma is collected and weighed. Since the flow rate into the nebulizer and time of collecting the waste is known, the total volume delivered to the nebulizer is also known. By subtracting the collected waste volume from this delivered volume, one obtains the volume that has entered the plasma.
The formula for the nebulization efficiency is then:

$$f_{neb} = \frac{\Delta\, total\ weight}{\Delta\, sample\ weight} \qquad (6.)$$

The method is inaccurate as it has a lot of uncertainties. The main problem is evaporation of the waste, which can make the calculated nebulization efficiency an overestimation. Subtracting two large numbers (when the nebulization efficiency is low) and inconsistency in waste drainage from the spray chamber also add uncertainty.

2. The particle frequency / particle number method:
When one assumes that each entering NP produces a signal, a standard suspension with known number concentration can be used to determine the nebulization efficiency. If the uptake rate is known, the number of NPs entering the nebulizer per second can be calculated and the number of peaks is assumed to be equal to the number of NPs reaching the plasma. This gives the following equation:

$$f_{neb} = \frac{N_{NP\ aerosol}}{N_{NP}} = \frac{f(I_p)}{q_{neb} \times c_p} \qquad (7.)$$

where $N_{NP\ aerosol\ /\ NP}$ = the number of NPs reaching the plasma / being delivered to the nebulizer.
While this method is the most direct, it is also the most unreliable in practice since there are no reference materials certified for number concentration and the number concentration in the very diluted suspensions suitable for spICP-MS might not be stable. NP suspensions are dynamic and so collisions between particles can result in aggregation (Verwey et al., 1999). NPs can also adhere to the walls of the container. Both effects reduce the actual number concentration in the standard, which would

lead to an overestimation of particles introduced and an underestimation of nebulization efficiency. This also leads to an underestimation of the particle size according to equation (2.).

3. *The particle size method:*
The currently most used method is the particle size method where the particle signals of a NP with a certified diameter are measured, and the nebulization efficiency in the following equation is then adjusted until the average particle mass calculated from the certified diameter is reproduced. The signal intensity of the solution is directly dependent on the nebulization efficiency and detection efficiency, but the signal intensity of particle events is not. Therefore, the nebulization efficiency is determined by the ratio of solution sensitivity to NP sensitivity, giving the following equation:

$$f_{neb} = \frac{I_{STD}/M_{STD}}{I_{NP}/M_{NP}} \quad (8.)$$

where $I_{STD/NP}$ = the signal intensity from the standard solution / NP and $M_{STD/NP}$ = mass of analyte in the standard solution / mass of analyte in the NP.
M_{STD} can be calculated according to equation (2.) and M_{NP} according to equation (4.):

$$M_{STD} = C_{STD} \times Q_{sample} \times t_{dwell}$$

$$M_{NP} = \frac{\rho \times \pi}{6} D_{NP}^3$$

One disadvantage of this method is that it relies on assumptions that might not always be valid. Besides the small inaccuracies in certified diameter, error might be introduced by that the density is assumed to be equal to the materials bulk density, despite some reports mentioning this isn't always the case. The NP shape of the standard is also assumed to be spherical, while metallic particles often are faceted.

1.3 Environmental spICP-MS applications

With the increasing use of ENPs in everyday consumer products, the release of these nanoparticles in the environment also rises, raising several questions about their toxicity on humans and the ecosystem. Numerous studies have shown the potential of spICP-MS to measure the concentration of ENPs in various environmental samples.

Tuoriniemi *et al.* (2012) investigated wastewater treatment plant (WWTP) effluent samples with spICP-MS. Out of the 13 screened elements (Ag, Ce, Ti, Si, Zn, Cr, Cu, Mo, Pt, Sb, W, Y and Zr), only Ag, Ce and Ti were detected, since they were most produced at that time. Their determined concentrations corresponded to the predicted values from environmental fate modelling. Yet, other frequently used NPs such as Zn and Si were not detected, most likely due to particle dissolution or lack of sensitivity. It was also concluded that the technique wasn't specific enough to differentiate between engineered Ti and Ce particles and the natural presence of these elements, so more research to optimize the technique is needed.
spICP-MS has also been used to investigate the detection of carbon nanotubes (CNTs) by Reed *et al.* (2013). CNTs are used in nanotechnology, electronics and optics, among other things and can thus enter the environment as industrial waste. Except for silver, they are used in more consumer products than any other ENP. It was found that the detection of these nanomaterials using residual catalyst metals (Co, Y, Mo or Ni) was possible with spICP-MS. CNTs could be detected at concentration in the ng/L range, which is lower than any other available technique. Despite spICP-MS not being able to detect most of the small metal masses used, which makes the technique only semi-quantitative, it was concluded that there are potential applications.

A study by Navratilova *et al.* (2015) used spICP-MS to successfully detect engineered CuO NPs in colloidal extracts from natural soil samples. The study compared sample dilution and dwell times to distinguish the CuO NPs against their high natural background. The natural background levels exceed the expected environmental concentrations of ENPs by several orders of magnitude, so it was concluded more research should and will be done to improve the method and thus detect even smaller NPs against higher Cu backgrounds in soils.
Another research, constructed by Peters *et al.* (2014) developed a method for sizing and determination of nano-silver in chicken meat. Ag NPs are the most used ENPs in consumer products, especially in food-related materials. This can result in an accumulation of Ag NPs in food. The developed method can be used to determine the presence and quantity of Ag NPs in the samples, with a LOD as low as 0,05 mg/kg. Peters *et al.* (2015) also used spICP-MS combined with a data evaluation tool for the analysis of NPs in complex matrices, such as food, waste water, culture media and biological tissues. spICP-MS was deemed an easy and fast technique for detection and characterization of metal and metal oxide NPs in these four complex samples, with no difficult sample preparation needed.

2 Experimental

A Perkin Elmer quadrupole ICP-MS (Nexion 350) operated through the Syngystix Nano app was used in all experiments. The ICP-MS settings are shown in table 1. The NP suspensions were prepared from citrate coated gold NP having nominal diameters of 5, 10, 20, 30, 40, 60 or 100 nm (BBI, UK) by diluting them with EDTA in ultrapure water (1000 mg L^{-1}). Dissolved Au standards were prepared from a 1000 mg L^{-1} Au standard by diluting with EDTA in ultrapure water (1000 mg L^{-1}). The nebulization efficiency was determined by using 60 nm Au NPs diluted 10^6 times.
For the digestions, all NPs except for the 30 nm ones were dissolved in aqua regia (65% HNO_3 (vol/vol) and 37% HCl (vol/vol)) and heated on a hot plate to a temperature close to the boiling point (90°C) for 30 minutes. The digestate was diluted 50 000 times in total (20 000 times in aqua regia and after digesting 20 times in 3% HCl) for the measurement. Each digestion set also included at least one blank sample and spike recovery sample.
Data analysis was done with Nanocount (Cornelis, 2014) and the peak detection program in Matlab (Tuoriniemi et al., 2015).

Table 1. *ICP-MS settings*

ICP-MS	Perkin Elmer Nexion 350
Spray chamber	Glass baffled (cyclonic)
Nebulizer	Glass expansion ca. 300 mL min^{-1} Micromist (conical)
Nebulizer gas flow rate	1.06 L min^{-1}
Plasma gas flow rate	18 L min^{-1}
Auxiliary gas flow rate	1.2 L min^{-1}
RF power	1600 W

DLS experiments were carried out on the Malvern Panalytical Zetasizer Nano ZS instrument.

3 Results and discussion

The Au NP dispersions with different sizes (5, 10, 20, 30, 40, 60 and 100 nm) were diluted to a concentration suitable for spICP-MS and measured to find the size and concentration detection limit.
All NPs except 30 nm were also digested and analysed by ICP-MS. This way, the total concentration Au was measured to calculate recovery during spICP-MS measurements.

3.1 5 nm - 10 nm - 20 nm

5, 10 and 20 nm particles were diluted 10^4 - 10^9 times and measured, but no NPs were detected. For particles of this size, the background intensity due to dissolved species is generally higher than the particle intensity, resulting in a low signal-to-background ratio. In the case of gold, reported size detection limits for a Perkin Elmer Nexion 350 are found to be 28 – 30 nm (Donovan et al., 2015).
The size DL is here defined as the NP size that can be distinguished from the continuous background noise fluctuations. It's dependent on the ITE, isotopic abundance, spectroscopic interference and dissolved analyte in the solution (Tuoriniemi et al., 2018). The ITE is instrument-specific and the abundance and interference are element-specific. For gold, relative low size DLs can thus be achieved, since the ^{197}Au isotope has 100% abundance and it's only interference is $^{181}Ta^{16}O^{+}$ (May and Wiedmeyer, 1998).
The standard deviation of a background in a blank was meant to be used. This is in theory the best-case DL that can be achieved with the instrument, though even the blank can contain particle events due to contamination and anomalies in the dissolved signal. Since it is the dissolved background signal in the sample itself that determines the detection limit for that particular sample, some arguments have been

made that the standard deviation should be taken from the sample itself and not the blank.

For these measurements of the particles, the nebulization efficiency was determined as 7.68%. Measurements were done with 10 µs dwell time, which were merged to 1 ms in Nanocount. Table 2. shows the detection limit calculated with equation (1.)

In practice, 2 counts is the smallest NP event detectable and a DL of 2 counts results in a size DL of 32.41 nm. This DL is also higher than the size of the measured particles, which affirms no NPs could be detected.

Table 2. *DLs for the measurement of 5, 10 and 20 nm Au NPs with 50 µs dwell time, calculated with equation (1.). Standard deviations obtained with Nanocount.*

Sample (*dilution*)	Standard deviation σ (counts)	n	DL (nm)
Blank	1.50	3	42.47
		5	50.35
10 nm (*10^5x*)	1.14	3	38.76
		5	45.95
20 nm (*10^4x*)	1.07	3	37.95
		5	44.99

3.2 30 nm

All 30 nm Au NP samples were diluted $4x10^6$ times. Measurements were done with 50 µs dwell times, which is 20 times shorter than the 1 ms used in the measurements. Overlap between dissolved and nanoparticle signal reduces as the dwell time is reduced, because the intensity of the dissolved signal increases with the dwell time, but the particle signal intensity does not. The duration of a particle event is typically ~ 500 µs, so the dwell time is shorter than the duration of a particle event (FAST). Only a fraction of a particle is measured during each dwell and the signal needs to be integrated to get the peak of the particle event. If the dwell time is significantly shorter than the duration of the ion burst, this will introduce dwells with no particle signal, so they are detected as different particle events instead of one. Because of this, no further improvement is made in DLs with dwell times below 200 - 100 µs.

With a nebulization efficiency of 1.29% and dwell time of 50 µs, the following DLs, shown in table 3., were obtained. The effect of the lower dwell time on the DL can be seen. As the dataset now mostly consists of zeros, the standard deviation becomes

extremely low, resulting in a DL that's impossibly small. The multiple of the standard deviation should be at least one to achieve a meaningful result and the DL calculated with equation (1.) doesn't take this into account.
There's a noticeable difference between the DL calculated with the blank or with a particle sample.

Table 3. *DLs for the measurement of 30 nm Au NPs with 50 µs dwell time, calculated with equation (1.). Standard deviations obtained with Nanocount.*

Sample (*dilution*)	Standard deviation σ (counts)	n	DL (nm)
Blank	0.0093	3	5.31
		5	6.29
30 nm 1 (10^6x)	0.23	3	15.46
		5	18.34
30 nm 2 (10^6x)	0.24	3	15.69
		5	18.60

In practice, the DL corresponding with 2 counts is 22.05 nm, which is a more believable result, because 20 nm particles could not be detected and the DL is therefore expected to be > 20 nm. This means the 30 nm NPs, which gave a signal with an intensity of 4 - 5 counts, were just distinguishable from the dissolved background. The total number concentration is 1.55 x 10^{13} particles mL^{-1}.

The PSD of the 30 nm Au NPs ($4x10^6$ times diluted) is shown in figure 7. There is a clear cut-off below 25 nm where the particle signal could not be resolved from the dissolved background.

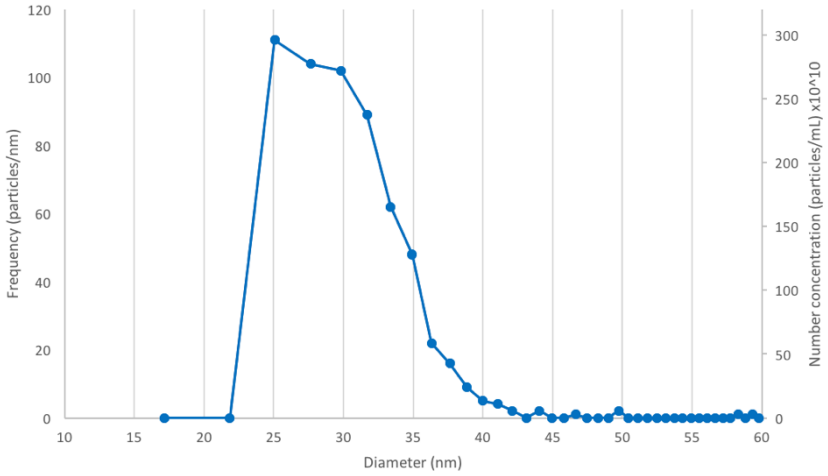

Figure 7. PSD of 30 nm Au NPs with 50 µs dwell time. X-axis shows diameter (nm), left y-axis shows frequency (particles nm^{-1}) and right y-axis shows number concentration (particles mL^{-1}) $x10^{10}$.

3.3 40 nm

The 40, 60 and 100 nm particles were all measured on the same day and thus have the same instrument sensitivity. All NPs were diluted 10^4 - 10^9 times and measured with 50 µs dwell time and a nebulization efficiency of 2.43%. The results for the DL is shown in table 3 below. Again, the DL based on the standard deviation of the blank is too low to be possible. The standard deviation of dissolved background was determined in Nanocount and depends on where the threshold is put, which explains the higher values for the 100 nm, where there's no overlap between the peak of dissolved background and particle events in the frequency – intensity histogram and the threshold can be placed higher. The DL for a particle consisting of only 2 counts is 22.74 nm.

Table 4. *DLs for the measurement of 40, 60 and 100 nm Au NPs with 50 µs dwell time, calculated with equation (1.). Standard deviations obtained with Nanocount.*

Sample (*dilution*)	Standard deviation σ (counts)	n	DL (nm)
Blank	0.055	3	9.90
		5	11.74
40 nm (10^4x)	0.88	3	24.94
		5	29.57
60 nm (10^5x)	0.47	3	20.24
		5	24.00
100 nm (10^4x)	1.97	3	32.63
		5	38.69

From the digestion was learned that the total gold concentration in the 40 nm samples is 47.83 mg L^{-1}. The recovery was calculated by determining the sum of the particle intensities in the outlier detection algorithm (in Matlab) and converting this to the total particle mass. As mentioned before, for dwell times below 100 µs, the fractions measured of a particle event during each dwell become so small the algorithm identifies them as a cluster of different peaks. This instrument has a relatively low acceleration voltage, making the duration over which one particle event spans rather ~ 750 – 1000 µs (based on the peak width of 60 and 100 nm NPs) instead of 500 µs. The background count rate comes close to zero and subsequently the multiple of the standard deviation turn out to be less than 1, which also makes the concept of outlier detection meaningless. Therefore, the dwells needed to be merged to bigger dwell times.
The sum of particle intensities was divided by the total sample volume used (= $f_{neb} \times t_{dwell} \times Q_{sample} \times$ total data points). This resulted in a concentration of 31.24 mg L^{-1}, which corresponds to a recovery of 65.31%.

A number concentration detection limit of three particle events has been proposed in literature (Laborda et al., 2013). This can be related to the limit of detection (LOD) with the nebulization efficiency (f_{neb}), sample flow rate (Q_{sample}) and total acquisition time (t_i), as seen in equation (9.) (Laborda et al., 2013).

$$LOD_{NP} = \frac{3}{f_{neb} \times Q_{sample} \times t_i} \quad (9.)$$

This LOD of 3 counts is based on an ideal Poisson distribution with a blank containing zero counts. The uncertainty due to finite particle count for 3 detected events in a 95% confidence interval would range between -80 to +292%. (Tuoriniemi et al., 2018).

Because the false positive rate in a sample differs from that in a blank or other reference sample and can only be estimated with uncerntainty, the number of particles counted for a reliable analysis must be even higher.

While this corresponds to LODs of ~ 10^5 particles L^{-1}, the total number of events counted must be at least 5 - 10 times higher for a PSD with maximum height of three events (based on an estimation done by Laborda *et al.* (2013) by considering a suspension of monodisperse NPs of the same diameter producing a Poisson distribution). This would be even higher if lognormal distributions, which are also often used for NP distributions, are used (Laborda et al., 2013). In practice LODs often approach ~ 10^6 particles L^{-1}.

For the measurements of 40, 60 and 100 nm, which had 50s total acquisition time and 0.7 mL min^{-1} flow rate, this results in a LOD of 211.64 particles mL^{-1} (2.1164 x 10^5 particles L^{-1}), which for 40 nm gold corresponds to 0.14 ng L^{-1} (when assuming the diameter is exactly 40 nm). This is at least ten times lower than actual reported LODs for 40 nm Au NPs, which are in the range of several ng L^{-1}. A certain number of large particles holds more mass. For the 40 nm NPs, enough particle events were measured to construct an accurate PSD in the samples that were 10^4 - 10^7 times diluted. Particle events had an intensity everywhere between 4 and 60 counts, with the most frequent intensity being 10/11 counts. The count rate was too low or the 10^8 - 10^9 times diluted (0.4783 ng L^{-1} and 0.04783 ng L^{-1}) samples. This affirms that the theoretical LOD is at least 10 times smaller than the LOD in practice.

A 95% confidence interval was calculated based on an equation published by Tuoriniemi *et al.* (2018). For the LOD of 3 particle events, the confidence interval is 0 – 35 740 particles mL^{-1}, which corresponds to 0 – 23.11 ng L^{-1} for 40 nm NPs, meaning the LOD can be even 100 times higher than 211.64 particles mL^{-1}.
This can't be directly related to how many particles are sufficient for a reliable PSD, since this also depends on PSD shape and width.

The total number concentration is 1.03 x 10^{12} particles mL^{-1}. Figure 8. shows the PSD of the 40 nm Au NPs (10^4 times diluted).

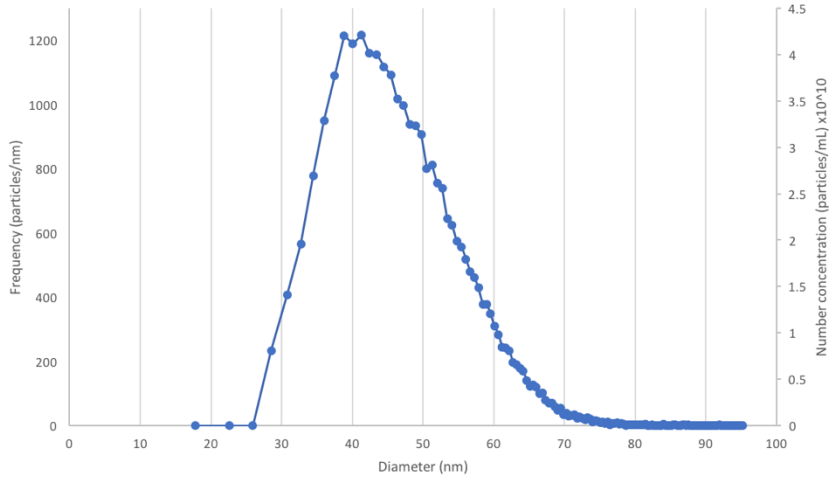

Figure 8. PSD of 40 nm Au NPs with 50 µs dwell time. X-axis shows diameter (nm), left y-axis shows frequency (particles nm^{-1}) and right y-axis shows number concentration (particles mL^{-1}) x10^{10}.

3.4 60 nm

The 60 nm NPs were characterized via dynamic light scattering (DLS), which measures the size distribution of particles in suspension. The average diameter is 60.27 nm.

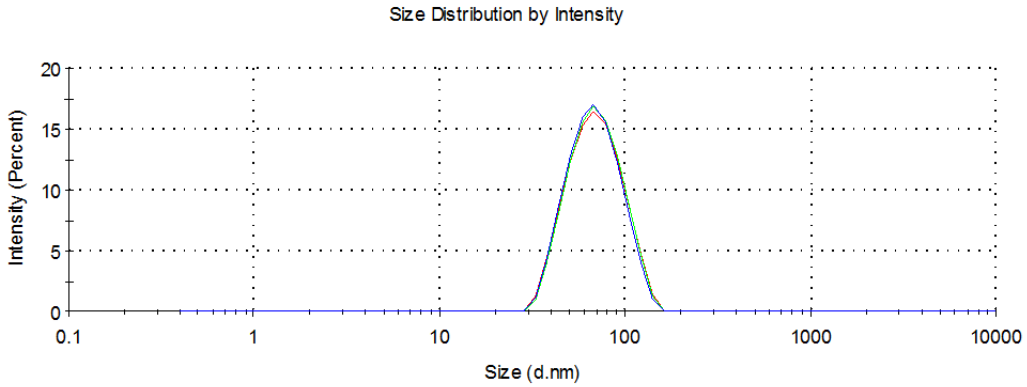

Figure 9. The DLS results for analysis of the 60 nm Au NPs.

The size DL has been shown in table 3. The total gold concentration for the 60 nm NPs as obtained by the digestion is 43.95 mg L^{-1}. The recovery of a 10^5 times diluted sample was calculated as 27.54 mg L^{-1}, which corresponds to a recovery of 62.66%.

The LOD of 211.64 particles mL^{-1} corresponds to 0.46 ng L^{-1} for 60 nm Au NPs. For samples that were 10^4 - 10^7 times diluted, enough particle events were measured, though 10^7 times diluted is not recommended due to inaccuracy because of low counting statistics. The particle events had an intensity span between ca. 15 and 90 counts, with 34 - 37 counts being the most frequent. For 10^8 - 10^9 times diluted, the count rate was too low. This corresponds with a concentration of 0.4783 ng L^{-1} – 0.04783 ng L^{-1}. The total number concentration is 4.87 x 10^{11} particles mL^{-1}.
The PSD of the 60 nm Au NPs (10^5 times diluted) is shown in figure 10.

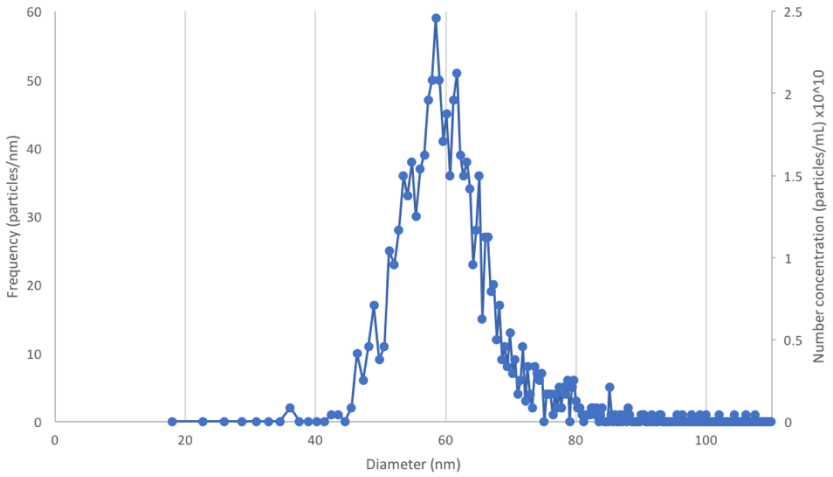

Figure 10. PSD of 60 nm Au NPs with 50 µs dwell time. X-axis shows diameter (nm), left y-axis shows frequency (particles nm^{-1}) and right y-axis shows number concentration (particles mL^{-1}) x10^{10}.

3.4.1 60 nm with spiked dissolved gold concentrations

60 nm Au NPs were diluted 10 000, 30 000, 60 000 and 90 000 times (4395 ng L^{-1}, 1465 ng L^{-1}, 733 ng L^{-1} and 488 ng L^{-1} respectively) and spiked with 0 ppb, 50 ppb and 75 ppb dissolved gold to increase the dissolved background signal. This mimics the presence of spectral interferences which are present for several elements often used in NPs and influence the size DL. There is already dissolved analyte present in most samples, but not in these high concentrations.

The 10 000 times diluted series is shown here. In outlier detection algorithm by Tuoriniemi *et al.* (2015) the n value is varied to see the effect on particle count obtained and size DL, as can be seen in figure 11 to 13. The smallest detectable size is calculated using $n*\sigma$ because the mean dissolved signal is subtracted from the particle signal intensities.

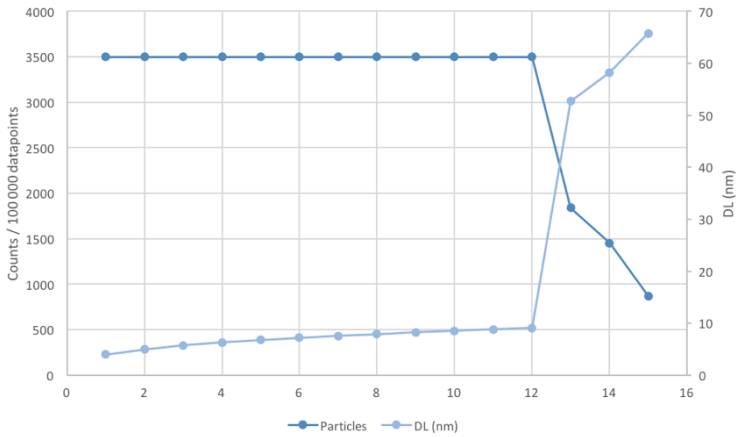

Figure 11. Particle count per 100 000 data points and size DL (nm) as a function of n parameter for 60 nm Au NPs measured with 50 µs dwell time and no spike added.

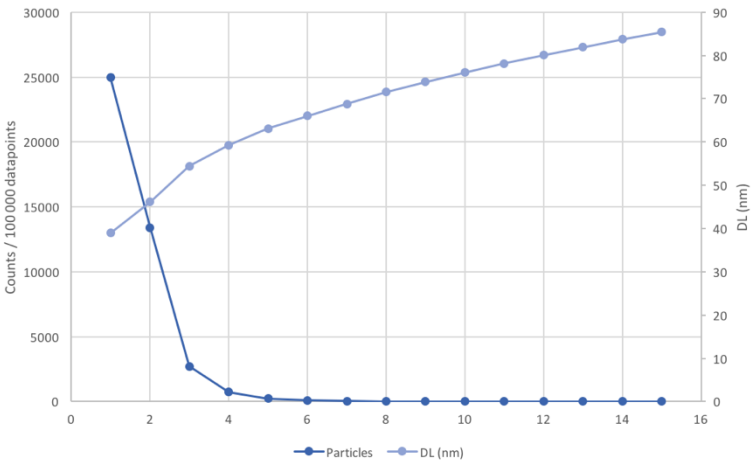

Figure 12. Particle count per 100 000 data points and size DL (nm) as a function of n for 60 nm Au NPs with 50 µs dwell time and 50 ppb spiked.

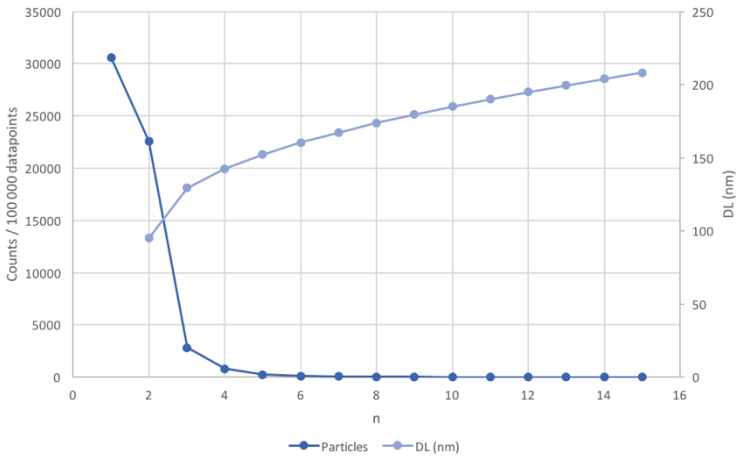

Figure 13. Particle count per 100 000 data points and size DL (nm) as a function of n for 60 nm Au NPs with 50 µs dwell time and 75 ppb spiked.

The size DL in the 60 nm particles without spike is extremely low because of the low background (0.04 counts) and all the particle events are completely separated from this background. In practice, a DL of 2 counts corresponds to 27.82 nm. From n = 12 to n = 13, the DL increases from 9.07 nm to 52.73 nm, indicating that actual particle events are considered as background. The dissolved background is ca. 0.25 ppb.

The 50 ppb dissolved standard (measured with 50 µs dwell time) was also analysed via this algorithm. The dissolved gold stock solution was measured via DLS and no evidence of significant particle concentrations were found. As shown in table 4, a value of n = 5 is needed to reduce the number of false positives to < 0.1% of the total count and get an accurate recovery (values are > 100 % because there is a dissolved background that's already present on top of the added 50 ppb). This corresponds to a background of 7.8 counts.

Table 5. *Results of particle count in 50 ppb dissolved standard with the outlier detection program with 100 000 dwells acquired in total.*

n	Particles counted	Background (counts)	Dissolved gold recovery (%)
1	32466	0.8825	10.60
2	6664	6.857	88.14
3	701	7.664	98.50
4	42	7.813	100.42
5	6	7.826	100.58

For the sample with 50 ppb spiked, the DL increases from 39.98 nm (n = 1) to 63.06 (n = 15) and for 75 ppb spiked this increases from 44.32 (n = 2) to 97.02 (n = 15). These DLs are very high, indicating that it was not possible to separate the dissolved background from the particle signal as there was too much overlap. The 50 ppb sample had a DL of 54.47 nm for n = 3 (background 6.2 counts) and 63.06 nm for n = 5 (background 6.9 counts). This is even higher for 75 ppb, which gave a DL of 60.32 nm for n = 3 (8.1 counts) and 70.96 nm for n = 5 (9.3). As the measured NPs are only 60 nm, this means only the end tail of the PSD can be distinguished. Except for the PSD of the sample with nothing spiked, the constructed PSDs gave incorrect size values of ~ 100 nm (50 ppb) and ~ 160 nm (75 ppb).

As can be seen in table 6., for a dissolved background that comes close to the added concentration of 50 and 75 ppb, the recovery is very poor. To get a dissolved background recovery of 100%, almost no particles will be detected. The added spiked concentrations almost completely mask the particle events, making it impossible to separate dissolved background from particle events.

Table 6. *Accuracy of the values obtained with different n*

Spike (ppb)	n	Background (counts)	Particle concentration (mg L^{-1})	Recovery (%)	Dissolved background (ppb)
50	3	6.187	22.98	52.28	39.76
	5	6.862	10.92	24.84	44.10
75	3	8.077	37.01	84.18	51.91
	5	9.305	14.73	33.54	59.80

3.5 100 nm

The 100 nm NPs were also characterized via DLS. The average measured diameter is 102.13 nm.

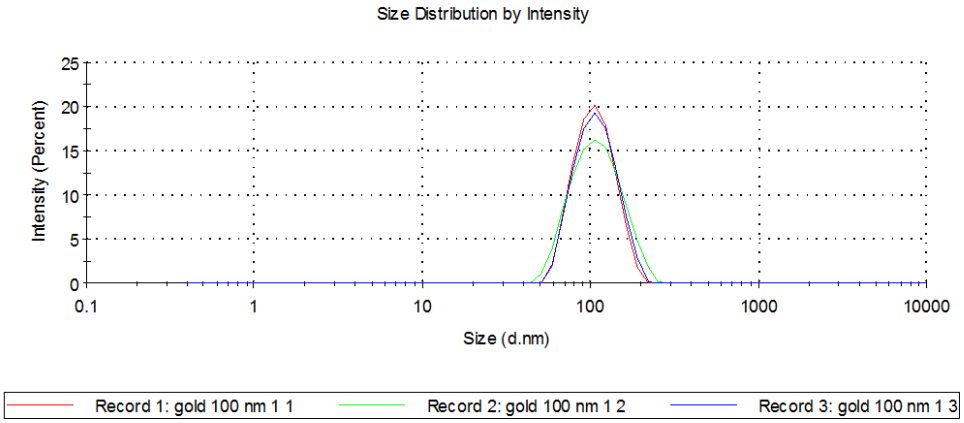

Figure 14. The DLS results for analysis of the 100 nm gold NPs

The size DL has been shown in table 3. As calculated from the digestion, the total 100 nm gold concentration 43.96 mg L^{-1}. The recovery of a 10^4 times diluted sample was calculated as 32.61 mg L^{-1}, which equals 74.18%.

The stated recoveries for the 40, 60 and 100 nm particles are based on the recoveries of the particle intensities. When calculating the total intensity, including the dissolved concentrations present, recoveries are on average 14% higher, meaning ca. 14% of the gold present in the dispersions was dissolved: 74.96% for 40 nm (~ 15% increase), 68.11% for 60 nm (~ 9% increase) and 86.55% for the 100 nm NPs (~ 17% increase). The count difference via the outlier detection program between the particle events intensities and the total intensity is for every sample higher than the dissolved background intensity subtracted in the raw data, indicating that at least some of the dissolved background surpassed the detection limit and was erronously counted as particle events.

The same calculated LOD of 211.64 particles mL^{-1} for 100 nm gold corresponds to 2.14 ng L^{-1}. Samples that were 10^4 - 10^6 times diluted gave good PSDs. As can be seen in the PSD of the 10^4 times diluted measurement, the intensity of a 100 nm NP is between ca. 100 - 300 counts, the most frequent intensities are 180 - 190 counts. For dilutions of 10^8 - 10^9 times (0.4396 ng L^{-1} - 0.04396 ng L^{-1}) no peaks of these intensities were obtained. 10^7x diluted (4.396 ng L^{-1}) is again at the tipping point: it

is above the theoretical LOD and a PSD can be constructed, but it's not precise and shouldn't be used. The number concentration is 1.45 x 10^{11} particles mL^{-1}. Figure 15 shows the PSD of the 100 nm Au NPs (10^4 times diluted).

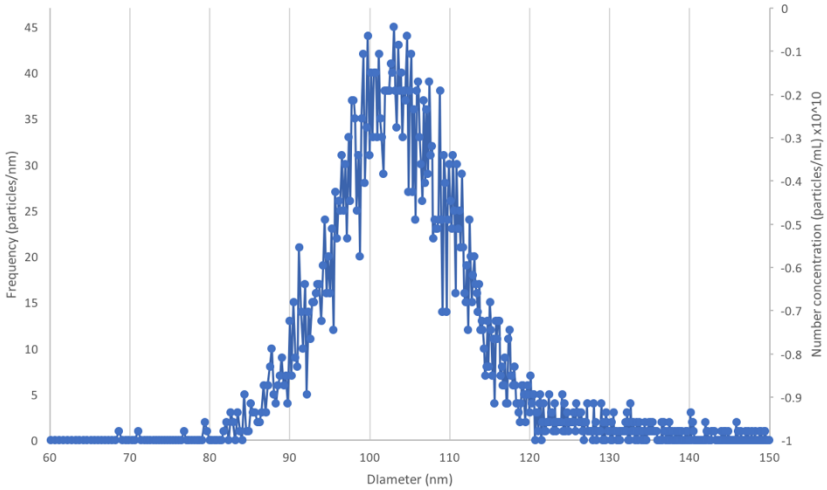

Figure 15. PSD of 100 nm Au NPs with 50 µs dwell time. X-axis shows diameter (nm), left y-axis shows frequency (particles nm^{-1}) and right y-axis shows number concentration (particles mL^{-1}) x10^{10}.

3.5.1 100 nm with 10 ms dwell times

Another measurement was performed, where the NPs were 10^5 - 10^{25} times diluted and measured with 10 ms dwell time. For a Q_{sample} = 0.25 mL min^{-1} and a f_{neb} = 7.68%, the LOD corresponds to 18.75 particles mL^{-1} or 0.1895 ng L^{-1} for 100 nm particles. The recovery here is 68.15%.

The size DLs are shown in table 7. They are quite high due to the longer dwell time. The DL corresponding to 2 counts is 25.61 nm. Figure 16. shows the PSD of the 100 nm Au NPs (10^5 times diluted), the number concentration is 1.5 x 10^{12} particles mL^{-1}. What sticks out is that this concentration is ten times higher than the number concentration of the 100 nm NPs measured with 50 µs dwell time. This is entirely due to the fact that the measurement with 50 µs dwell time was done more than two months after the measurement with 10 ms. Besides the fact that the particles with 50 µs dwell time had 60% more total volume, thus resulting in lower number concentration, this can also be explained by the difference in time. Particle suspensions are dynamic and the measurement with 50 µs was done more than two months after the measurement with 10 ms. Some NPs were probably dissolved, adsorbed into the

tube walls or enlarged due to Ostwald ripening, thus becoming too big for detection with spICP-MS. This leads to a lower concentration of particles present in the sample.

Table 7. *DLs for the measurement of 100 nm Au NPs with 10 ms dwell time, calculated with equation (1.). Standard deviations obtained with Nanocount.*

Sample (*dilution*)	Standard deviation σ (counts)	n	DL (nm)
Blank	1.248	3	31.53
		5	37.38
100 nm (10^5x)	1.265	3	31.67
		5	37.55

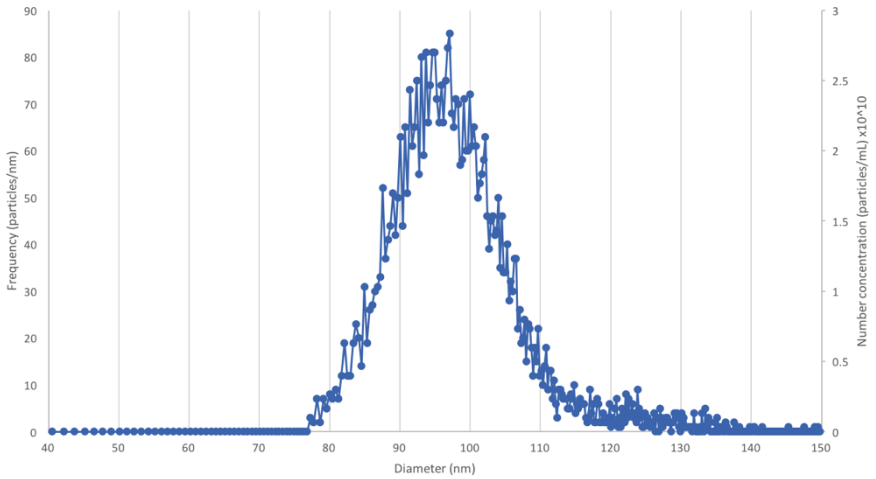

Figure 16. PSD of 100 nm Au NPs with 10 ms dwell time. X-axis shows diameter (nm), left y-axis shows frequency (particles nm^{-1}) and right y-axis shows number concentration (particles mL^{-1}) $x10^{10}$

The parameter n in the outlier detection program is again varied against particle count and size DL of the most concentrated (10^5 times diluted) sample, as can be seen in figure 17. The obtained size DLs via this algorithm are higher than the DLs via equation (1.) The longer dwell time results in a higher background, for n = 1 the background is 2.39 counts, which corresponds with a DL of 30.13 nm.

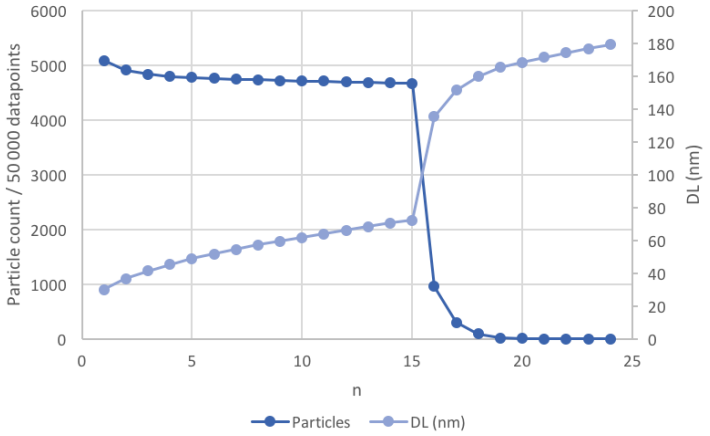

Figure 17. Particle count per 50 000 datapoints and size DL (nm) as a function of n for 100 nm Au NPs 10^5x diluted (10 ms dwell time).

The biggest changes happen for n < 5, after n = 5, which corresponds with a DL of 48.89 nm, the particle count and DL only increase slightly. After n = 15, the particle count drops from ca. 4700 to 1000 particles per 50 000 datapoints and the DL increases from 72.41 nm to 135.43 nm. This means that for n > 15, the false negative count is very high, almost all 100 nm NPs are erroneously considered as background.

Figure 19. shows the same graph, but on a 100 nm sample that is 10^{25} times diluted. Because of this large dilution, almost no NP events will be present and the raw data shows that maximum one NP event is detected. This means almost all particles counted are false positives. For n = 3, ca. 1200 particles are counted and the DL is 28.08 nm. Between n = 5 (49 particles counted, DL = 33.67 nm) which counts 0.098% of false positives and n = 7 (3 particles counted, DL = 37.17 nm), 0.006% of false positives almost no background is counted as a particle. After that the DL keeps increasing, to levels where particles are no longer detected in the sample.

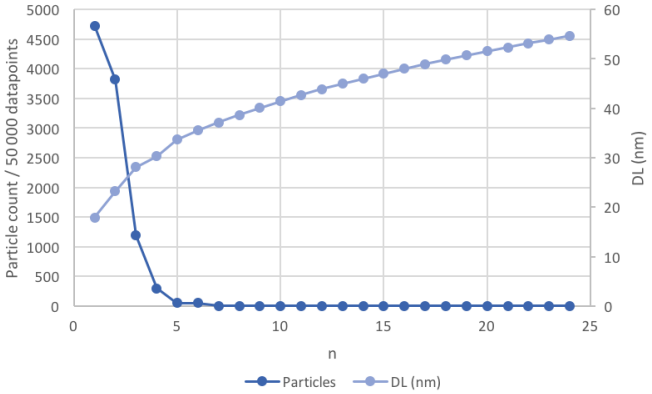

Figure 19. Particle count per 50 000 datapoints and size DL (nm) as a function of n for 100 nm Au NPs 10^{25}x diluted (10 ms dwell time).

3.6 Effect of dwell time on signal

100 ppb was measured with different dwell times to see how accurate the detector operates under the different dwell times. The results of one measurement are shown in the table below. The intensity in CPS stays constant, with a deviation of 2.45% and 3.80% for a second measurement. This proves that the detector behaves as it should, even down to the shortest dwell times.

The longer the dwell time, the shorter the variation in intensity. For this reason, longer dwell times were originally considered to be more accurate. However, recent research has proven that longer dwell times give a greater possibility of coincidence and shorter dwell times allow better particle resolution in the case of spICP-MS.

Table 8. *The average intensity of 100 ppb dissolved gold at different dwell times*

Dwell time	Average intensity (CPS)	Relative variance intensity (%)
10 µs	585 292	44.27
20 µs	565 665	33.17
50 µs	574 769	24.39
70 µs	568 850	21.73
100 µs	545 439	19.93
200 µs	554 570	16.55
1000 µs	560 294	11.85
5000 µs	550 122	9.80
10 000 µs	545 023	12.00
Deviation	2,46 %	

4 Conclusion

The particle size detection limit has been found to vary between 22 and 32 nm for an Au particle to produce 2 ions, the smallest detectable particle event. As can be seen in table 9., the DL increased with the dwell time, but is also dependent on the instrument sensitivity on that day. The overlap between dissolved and nanoparticle signal reduces as the dwell time is reduced.
Equation (1.) by Lee *et al.* (2014) gave results that varied a lot between measurements. The measurements with 10 ms dwell time resulted in DLs that seem reasonable, albeit a bit high. However, when 50 µs dwell times are used, the standard deviation of the blank becomes so low that DLs of ~ 10 nm were obtained, while it should be > 20 nm, as no NPs below this size were detected. In this case, the DLs calculated with the standard deviation of the background in the samples were more correct, though there was some variation between samples used.
When using FAST, further improvement of size DLs is rather limited by the ITE of the instrument than the dissolved concentration. Sector field instruments, which are found to be more sensitive than quadrupole mass spectrometers, even have reported size DLs of 6 nm for Au NPs (Tuoriniemi et al., 2015).

Dwell times of 50 µs also needed to be merged to bigger dwell times to get correct values in the outlier detection algorithm, as the outlier detection program can't be used for a multiple of the standard deviation that's less than 1.
There was a ca. 15% variation between the DL obtained with a 3σ or 5σ threshold. The 5σ threshold seemed to be too conservative, the 3σ threshold was often closer to the DL corresponding with 2 counts.

In general, calculating the DL from a minimum intensity of 2 counts seemed to be a reliable and fast way of calculating the DL, more so than basing the DL on equation (1.).

The theoretical concentration LOD based on equation (9.) (0.14 ng L^{-1} for 40 nm, 0.46 ng L^{-1} for 60 nm and 2.14 ng L^{-1} for 100 nm) was in all cases at least 10 times smaller than the LOD in practice, which was in the range of several ng L^{-1} for the 40 nm particles and rather ~ 40 ng L^{-1} for an accurate PSD of the bigger 60 and 100 nm particles.

Table 9. *Summary of the resulted DL, number concentration and recovery for each particle size.*

Size (nm)	Dwell time (μs)	DL (nm) for 2 counts	Number concentration (particles mL^{-1})	Recovery (%)
5	1000	32.41	-	-
10	1000	32.41	-	-
20	1000	32.41	-	-
30	50	22.05	1.55×10^{13}	-
40	50	22.74	1.03×10^{12}	65.31
60	50	22.74	4.87×10^{11}	62.66
60 (spiked)	50	27.82	-	-
100	50	22.74	1.45×10^{11}	74.18
100	10 000	25.58	1.50×10^{12}	68.15

Recoveries varied between 60 – 70% and depend on the instrument and sample preparation. Ca. 13% of the total gold present was dissolved, with some dissolved intensities even surpassing the DL.
The number concentration decreases with increasing size, since for the same mass one gets a higher number of small particles than big particles.
The two measurements of 100 nm NPs showed that the particle suspensions are still very dynamic and the measured number concentration can decrease quite drastically over time due to artefacts such as Ostwald ripening, adsorption to the tube walls or the particles simply dissolving.

Validation of the outlier detection algorithm parameters has been done. The value of n = 5 seemed to be more appropriate than n = 3: the size DL is higher but still smaller than the actual particle size, so the rate of false positives is not too high. After a n value of 5, there is little change in particle count and size DL. Higher values do not automatically correspond to better results, as for $n \geq 15$ actual particles are counted as background.
In the very dilute sample, the 3σ threshold still counted 2.4% as false positives. The 5σ threshold was accurate enough to be used, with only 0.098% of false positives. Increasing the n value to 7 gave even better results (0.006% of false positives), but $n > 7$ values gave no further improvement.

It was impossible to separate the 60 nm Au NPs from the spiked 50 and 75 ppb dissolved background since the concentration was too high and almost completely masks the particle intensities. Only the upper tail of the PSD could be resolved, resulting in sizes that were bigger than the actual size. The DL increased with increased added dissolved concentration.

Regardless of the dwell time used, the intensity in CPS stays constant, so no problems with the detector should be expected. Smaller dwell times do result in bigger intensity variations, which can lead to some inaccuracies.

Further research to detect NPs in the presence of high dissolved backgrounds is required, as well as research for DLs and LODs of other types of nanoparticles, such as NPs with different isotopes and / or spectral interferences. Despite these shortcomings, spICP-MS has shown to be very promising for future quantification of nanoparticles in environmental media.

References

BI, X., LEE, S., RANVILLE, J. F., SATTIGERI, P., SPANIAS, A., HERCKES, P. & WESTERHOFF, P. 2014. Quantitative resolution of nanoparticle sizes using single particle inductively coupled plasma mass spectrometry with the K-means clustering algorithm. *Journal of Analytical Atomic Spectrometry,* 29**,** 1630-1639.

BOULYGA, S. F. & BECKER, J. S. 2002. Improvement of abundance sensitivity in a quadrupole-based ICP-MS instrument with a hexapole collision cell. *Journal of Analytical Atomic Spectrometry,* 17**,** 1202-1206.

BOYSEN, E. & BOYSEN, N. M. 2018. *Nanoparticle Applications and Uses* [Online]. Hawk's Perch Technical Writing. Available: http://www.understandingnano.com/nanoparticles.html [Accessed].

BUSTOS, A. R. M. & WINCHESTER, M. R. 2016. Single-particle-ICP-MS advances. *Analytical and Bioanalytical Chemistry,* 408**,** 5051-5052.

CHEN, W. C., WEE, P. & BRINDLE, I. D. 2000. Elimination of the memory effects of gold, mercury and silver in inductively coupled plasma atomic emission spectroscopy. *Journal of Analytical Atomic Spectrometry,* 15**,** 409-413.

CORNELIS, G. 2014. Nanocount. Gothenburg: Gothenburg University.

CORNELIS, G. & HASSELLOV, M. 2014. A signal deconvolution method to discriminate smaller nanoparticles in single particle ICP-MS. *Journal of Analytical Atomic Spectrometry,* 29**,** 134-144.

DEGUELDRE, C. & FAVARGER, P. Y. 2003. Colloid analysis by single particle inductively coupled plasma-mass spectroscopy: a feasibility study. *Colloids and Surfaces a-Physicochemical and Engineering Aspects,* 217**,** 137-142.

DEGUELDRE, C. & FAVARGER, P. Y. 2004. Thorium colloid analysis by single particle inductively coupled plasma-mass spectrometry. *Talanta,* 62**,** 1051-1054.

DEGUELDRE, C., FAVARGER, P. Y. & BITEA, C. 2004. Zirconia colloid analysis by single particle inductively coupled plasma-mass spectrometry. *Analytica Chimica Acta,* 518**,** 137-142.

DEGUELDRE, C., FAVARGER, P. Y., ROSSE, R. & WOLD, S. 2006a. Uranium colloid analysis by single particle inductively coupled plasma-mass spectrometry. *Talanta,* 68**,** 623-628.

DEGUELDRE, C., FAVARGER, P. Y. & WOLD, S. 2006b. Gold colloid analysis by inductively coupled plasma-mass spectrometry in a single particle mode. *Analytica Chimica Acta,* 555**,** 263-268.

DONOVAN, A. R., SHI, H., ADAMS, C., STEPHAN, C. & MONITORING, S. M. 2015. Rapid Analysis of Silver, Gold, and Titanium Dioxide Nanoparticles in Drinking Water by Single Particle ICP-MS. *PerkinElmer application note*.

EUROPEANCOMMISSION. 2017. *Definition of a Nanomaterial* [Online]. Available: http://ec.europa.eu/environment/chemicals/nanotech/faq/definition_en.htm [Accessed].

GALLEGO-URREA, J. A., TUORINIEMI, J., PALLANDER, T. & HASSELLOV, M. 2010. Measurements of nanoparticle number concentrations and size distributions in contrasting aquatic environments using nanoparticle tracking analysis. *Environmental Chemistry,* 7**,** 67-81.

HANDY, R. D., OWEN, R. & VALSAMI-JONES, E. 2008. The ecotoxicology of nanoparticles and nanomaterials: current status, knowledge gaps, challenges, and future needs. *Ecotoxicology,* 17**,** 315-325.

HASSELLÖV, M., READMAN, J. W., RANVILLE, J. F. & TIEDE, K. 2008. Nanoparticle analysis and characterization methodologies in environmental risk assessment of engineered nanoparticles. *Ecotoxicology,* 17**,** 344-361.

KUTSCHER, D., WILLS, J. D. & DUCOS, S. M. 2018. Nanoparticle Characterization Via Single Particle Inductively Coupled Plasma-Mass Spectrometry (spICP-MS) Using a Dedicated Plug-in for Qtegra ISDS Software. *Technical note 43279.* Germany: Thermo Fisher Scientific.

LABORDA, F., JIMENEZ-LAMANA, J., BOLEA, E. & CASTILLO, J. R. 2013. Critical considerations for the determination of nanoparticle number concentrations, size and number size distributions by single particle ICP-MS. *Journal of Analytical Atomic Spectrometry,* 28**,** 1220-1232.

LEE, S., BI, X., REED, R. B., RANVILLE, J. F., HERCKES, P. & WESTERHOFF, P. 2014. Nanoparticle Size Detection Limits by Single Particle ICP-MS for 40 Elements. *Environmental Science & Technology,* 48**,** 10291-10300.

LIAS, S. G. & LIEBMAN, J. F. 2018. Ion Energetics Data. *In:* LINSTROM, P. J. & MALLARD, W. G. (eds.) *NIST Chemistry WebBook, NIST Standard Reference Database Number 69.* Gaithersburg MD: National Institute of Standards and Technology.

MAY, T. W. & WIEDMEYER, R. H. 1998. A table of polyatomic interferences in ICP-MS. *Atomic Spectroscopy,* 19**,** 150-155.

MITRANO, D. M., LESHER, E. K., BEDNAR, A., MONSERUD, J., HIGGINS, C. P. & RANVILLE, J. F. 2012. Detecting nanoparticulate silver using single-particle inductively coupled plasma–mass spectrometry. *Environmental Toxicology and Chemistry,* 31**,** 115-121.

MONTANO, M. D., BADIEI, H. R., BAZARGAN, S. & RANVILLE, J. F. 2014. Improvements in the detection and characterization of engineered nanoparticles using spICP-MS with microsecond dwell times. *Environmental Science: Nano,* 1**,** 338-346.

MONTANO, M. D., OLESIK, J. W., BARBER, A. G., CHALLIS, K. & RANVILLE, J. F. 2016. Single Particle ICP-MS: Advances toward routine analysis of nanomaterials. *Anal Bioanal Chem,* 408**,** 5053-74.

MONTASER, A. 1998. *Inductively Coupled Plasma Mass Spectrometry*, Wiley.

NAVRATILOVA, J., PRAETORIUS, A., GONDIKAS, A., FABIENKE, W., VON DER KAMMER, F. & HOFMANN, T. 2015. Detection of Engineered Copper Nanoparticles in Soil Using Single Particle ICP-MS. *International Journal of Environmental Research and Public Health,* 12**,** 15756-15768.

NEL, A., XIA, T., MENG, H., WANG, X., LIN, S., JI, Z. & ZHANG, H. 2012. Nanomaterial toxicity testing in the 21st century: use of a predictive toxicological approach and high-throughput screening. *Accounts of chemical research,* 46**,** 607-621.

PACE, H. E., ROGERS, N. J., JAROLIMEK, C., COLEMAN, V. A., HIGGINS, C. P. & RANVILLE, J. F. 2011. Determining Transport Efficiency for the Purpose of Counting and Sizing Nanoparticles via Single Particle Inductively Coupled Plasma Mass Spectrometry. *Analytical Chemistry,* 83**,** 9361-9369.

PETERS, R., HERRERA-RIVERA, Z., UNDAS, A., VAN DER LEE, M., MARVIN, H., BOUWMEESTER, H. & WEIGEL, S. 2015. Single particle ICP-MS combined with a data evaluation tool as a routine technique for the analysis of nanoparticles in complex matrices. *Journal of Analytical Atomic Spectrometry,* 30**,** 1274-1285.

PETERS, R. J. B., RIVERA, Z. H., VAN BEMMEL, G., MARVIN, H. J. P., WEIGEL, S. & BOUWMEESTER, H. 2014. Development and validation of single particle ICP-MS for sizing and quantitative determination of nano-silver in chicken meat. *Analytical and Bioanalytical Chemistry,* 406**,** 3875-3885.

REED, R. B., GOODWIN, D. G., MARSH, K. L., CAPRACOTTA, S. S., HIGGINS, C. P., FAIRBROTHER, D. H. & RANVILLE, J. F. 2013. Detection of single walled carbon nanotubes by monitoring embedded metals. *Environmental Science-Processes & Impacts,* 15**,** 204-213.

THOMAS, R. 2001a. A beginner's guide to ICP-MS - Part IV: The interface region. *Spectroscopy,* 16**,** 26-+.
THOMAS, R. 2001b. *Beginner's guide to ICP-MS - Part VI - The mass analyzer*.
THOMAS, R. 2001c. Spectroscopy tutorial - A beginner's guide to ICP-MS - Part I. *Spectroscopy,* 16**,** 38-+.
THOMAS, R. 2001d. Spectroscopy tutorial - A beginner's guide to ICP-MS - Part II: The sample-introduction system. *Spectroscopy,* 16**,** 56-+.
THOMAS, R. 2002. A beginner's guide to ICP-MS part X - Detectors. *Spectroscopy,* 17**,** 34-+.
TUORINIEMI, J., CORNELIS, G., BADIEI, H. & HASSELLÖV, M. 2018. Nanoparticle Characterization Using Single Particle ICP-MS. Gothenburg.
TUORINIEMI, J., CORNELIS, G. & HASSELLOV, M. 2015. A new peak recognition algorithm for detection of ultra-small nano-particles by single particle ICP-MS using rapid time resolved data acquisition on a sector-field mass spectrometer. *Journal of Analytical Atomic Spectrometry,* 30**,** 1723-1729.
TUORINIEMI, J., CORNELIS, G. & HASSELLÖV, M. 2012. Size discrimination and detection capabilities of single-particle ICP-MS for environmental analysis of silver nanoparticles. *Analytical Chemistry,* 29**,** 743-752.
TUORINIEMI, J., CORNELIS, G. & HASSELLÖV, M. 2014. Improving Accuracy of Single particle ICPMS for Measurement of Size Distributions and Number Concentrations of Nanoparticles by Determining Analyte Partitioning during Nebulisation. *Journal of Analytical Atomic Spectrometry,* 29**,** 743-752.
VANHAECKE, F. Spectroscopische analysemethoden: ICP-Massaspectrometrie. Lecture notes, 2017 Belgium. Universiteit Gent.
VERWEY, E. J. W., OVERBEEK, J. T. G. & OVERBEEK, J. T. G. 1999. *Theory of the stability of lyophobic colloids*, Courier Corporation.
WESTERHOFF, P. & NOWACK, B. 2012. Searching for global descriptors of engineered nanomaterial fate and transport in the environment. *Accounts of chemical research,* 46**,** 844-853.
WIESNER, M. R., LOWRY, G. V., ALVAREZ, P., DIONYSIOU, D. & BISWAS, P. 2006. Assessing the risks of manufactured nanomaterials. ACS Publications.

Acknowledgements

Massive thanks go out to Geert Cornelis and Jani Tuoriniemi, for always being prepared to answer my many questions, always staying optimistic and dedicating so much time to guiding me through this thesis.